Journal of Fluids and Structures 27 (2011) 1182–1198

Contents lists available at ScienceDirect

Journal of Fluids and Structures

journal homepage: www.elsevier.com/locate/jfs

Power extraction from aeroelastic limit cycle oscillations

J.A. Dunnmon *, S.C. Stanton, B.P. Mann, E.H. Dowell

Department of Mechanical Engineering and Materials Science, Duke University, Durham, NC 27708-0300, USA

ARTICLE INFO

Article history:
Received 19 August 2010
Accepted 15 February 2011
Available online 16 March 2011

Keywords:
Aeroelasticity
Energy harvesting
Piezoelectricity

ABSTRACT

Nonlinear limit cycle oscillations of an aeroelastic energy harvester are exploited for enhanced piezoelectric power generation from aerodynamic flows. Specifically, a flexible beam with piezoelectric laminates is excited by a uniform axial flow field in a manner analogous to a flapping flag such that the system delivers power to an electrical impedance load. Fluid–structure interaction is modeled by augmenting a system of nonlinear equations for an electroelastic beam with a discretized vortex-lattice potential flow model. Experimental results from a prototype aeroelastic energy harvester are also presented. Root mean square electrical power on the order of 2.5 mW was delivered below the flutter boundary of the test apparatus at a comparatively low wind speed of 27 m/s and a chord normalized limit cycle amplitude of 0.33. Moreover, subcritical limit cycles with chord normalized amplitudes of up to 0.46 were observed. Calculations indicate that the system tested here was able to access over 17% of the flow energy to which it was exposed. Methods for designing aeroelastic energy harvesters by exploiting nonlinear aeroelastic phenomena and potential improvements to existing relevant aerodynamic models are also discussed.

1. Introduction

The research literature pertaining to aeroelastic energy harvesting is increasing in view of the shortcomings of small-scale rotary generators (Mitcheson et al., 2008). Furthermore, small-scale devices capable of extracting energy from flow fields may enable future development of micro-aerial-vehicles (De Marqui et al., 2010), wireless sensor networks (Bryant et al., 2009), distributed generation schemes, and other revolutionary engineering systems dependent on small, but crucial amounts of localized electrical power. Vibration based energy harvesting has significant potential in these applications not only due to the availability and continued development of effective small-scale transducers (Sodano et al., 2004), but also because of the ease with which systems can be designed to vibrate in ambient environmental conditions (Eichorn et al., 2008). Given the current governmental and industrial emphases on carbon free energy, power system minimization, and decentralized generation, the development of vibratory energy harvesters is a logical and valuable technological step (Lindsey, 2002).

A particularly fruitful source of environmentally excited vibrations can be found in various modes of fluid–structure interaction. Myriad systems that take advantage of such vibrations have already been conceptualized and, in some cases, convincingly tested. Concepts ranging from small diaphragms in pressurized flow channels (St Clair et al., 2010) to the large scale vortex induced vibration (VIV) based harvesters of Bernitsas et al. (2008) have been recently investigated.

* Corresponding author. Tel.: +1 513 477 8441; fax: +1 919 660 8963.
E-mail addresses: jared.dunnmon@duke.edu (J.A. Dunnmon), scs23@duke.edu (S.C. Stanton), brian.mann@duke.edu (B.P. Mann), dowell@ee.duke.edu (E.H. Dowell).

0889-9746/$ - see front matter
doi:10.1016/j.jfluidstructs.2011.02.003

Excitation methodologies have varied from inducing oscillations in a flexible duct wall (Wang and Ko, 2010) to utilizing vortex shedding from a bluff body to excite motion in a downstream apparatus (Akaydin et al., 2009).

Erturk et al. (2010) have experimentally demonstrated the potential of utilizing fluid–structure interaction to harvest energy from ambient airflow by extracting power on the order of 10 mW from relatively low speed flow using small cantilevered piezoelectric elements in combination with external system excitation by means of a gust generator. De Marqui's investigation of the concept of a generator wing, in a similar fashion, has shed light on the significant influence of both aerodynamic damping and flow speed regime on the effectiveness of piezoelectric energy transduction from such a system. In particular, it appears that operating a system at or slightly above its linear flutter speed is ideal for efficient power extraction from many externally excited systems (De Marqui et al., 2010).

The cantilevered beam in axial flow is a system often targeted for use in aeroelastic energy harvesters due to its conceptual simplicity, known behavioral characteristics, and ease of manufacture. The energy harvesting eel of Taylor et al. (2001) takes advantage of the useful attributes of this system in a marine environment to produce significant amounts of power at relatively low flow speeds. Bryant et al. (2009) have taken a further step toward practical application of this technology by designing a low speed aeroelastic energy harvester that produces up to 2 mW at wind speeds under 2.5 m/s. The Bryant harvester, which utilizes passive electrical load optimization based on weak piezoelectric coupling, is a two degree of freedom system incorporating flow induced motion in both pitch and plunge vibration modes. The use of a flat plate as opposed to a standard airfoil for the aeroelastic section was investigated, with the major result being that the flat plate provided more consistent power levels over a spectrum of wind speeds while the airfoil allowed for certain resonance phenomena to occur, causing higher peak power levels (Bryant et al., 2009).

Tang et al. (2009) have recently studied flow energy extraction with a flexible energy harvester inspired by flapping flag dynamics. They have shown through detailed energy transfer models that the output of devices based on such a system could in fact rival that of traditional horizontal axis wind turbines if implemented on a large scale (Tang et al., 2009). Such a conclusion is crucial to validating the continued investigation of aeroelastic energy harvesting systems for both microscale and macroscale applications. Moreover, the current work of Kimber et al. (2009) reflects encouragingly on the potential for enhancing the operation of these systems through utilization of constructive mutual interaction between collocated flapping flags in the design of aeroelastic energy harvesting arrays.

An aspect of the aeroelastic energy harvester that has not yet been fully examined in a design context, however, is the existence of key aeroelastic nonlinearities that often lead to large amplitude self-excited limit cycle oscillations (LCO) at flow velocities above, and occasionally below, the linear flutter speed. This paper seeks to both theoretically and experimentally address the influence of nonlinear aeroelastic response on the energy harvesting potential of a cantilevered plate with piezoelectric laminates for energy conversion. Effectively accessing the energy contained in the limit cycles that so often occur in these systems could ultimately be crucial to designing aeroelastic energy harvesters that take full advantage of the unique dynamic properties of the flapping flag. Not only could the extremely large amplitudes characteristic of these LCO greatly increase the efficacy of piezoelectric transduction, but the ability to design self-excited energy harvesters that do not require external forcing to reach large amplitudes could greatly improve the effectiveness and practicality of this particular aeroelastic energy harvesting paradigm.

This paper addresses these issues first theoretically by describing a simple vortex-lattice discretization of the aerodynamic system used to model the flow around a cantilevered flexible plate. An augmentation to the canonical structural model is then derived in order to integrate the electrodynamics of the energy harvester into the classical aeroelastic state space equations, forming what is henceforth termed the aeroelectroelastic model. The construction of a rudimentary LCO based energy harvester and subsequent wind tunnel experimentation is described. Visual and empirical data from these experiments are analyzed in order to characterize the performance of the system both in terms of energy harvesting potential and degree of adherence to the simplified aeroelectroelastic model. Finally, various relevant efficiency measures are calculated in order to further characterize the system in the context of harvesting ambient flow energy.

2. Theoretical modeling

The aeroelastic harvester studied in this paper is shown in Fig. 1. The device consists of a flat cantilevered elastic panel with piezoelectric laminates attached in a bimorph configuration. The panel has width b, length L, and thickness t. Fixed boundary conditions at the base of the beam are achieved by clamping its leading edge to a rigid airfoil of width $b_{\text{foil}} \gg b$ and length L_0. Accordingly, the chord length of the harvester is defined as $L+L_0$.

The device itself is designed to harvest energy from self-excited LCO in axial airflow. A rigid airfoil mounted vertically in a wind tunnel is used to cantilever a thin aluminum plate parallel to the direction of airflow. When wind speed reaches the critical flow velocity at which aeroelastic damping becomes negative, large amplitude LCO are induced. A piezoelectric transducer placed near the root of the cantilevered beam is then used to extract electrical power from the strain caused by the large amplitude oscillation. The transducer circuitry consists of a piezoelectric bimorph coupled to a simple impedance load. Oscillation amplitude can be tuned to desired levels by adjusting air speed while electrical properties can be adjusted by changing the resistance value of the impedance load. Power is measured by recording voltage and impedance across the load. Such a device allows for the effective investigation of this system in terms of physical behavior, electromechanical coupling, and energy harvesting potential.

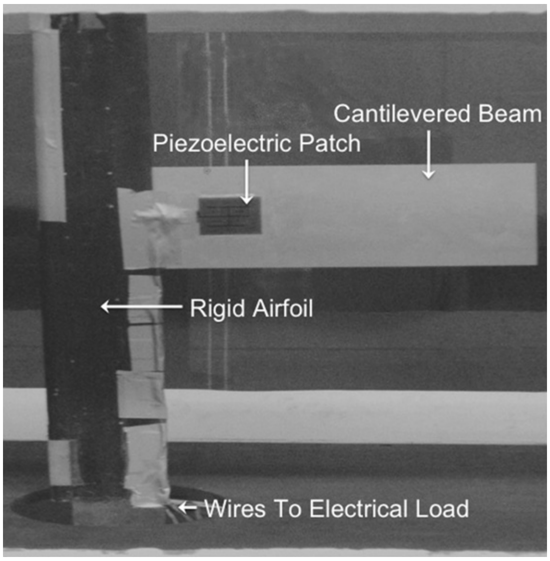

Fig. 1. Image of experimental setup.

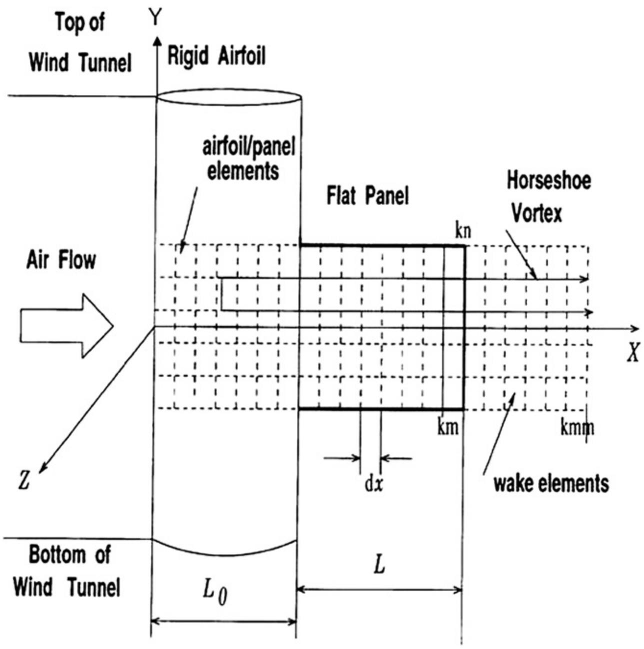

Fig. 2. Schematic of an aerodynamic vortex-lattice framework of the system.

2.1. Aerodynamic model

To fully understand this system, it is necessary that one not only observe its behavior, but also understand the intrinsic dynamics to the point that experimental behavior can be accurately predicted. The first step in this process is to form a basic theoretical conception of the aerodynamics involved in this system. The aerodynamic model utilized here is a linear, unsteady, three-dimensional vortex-lattice framework for irrotational, inviscid, and incompressible flows. Following Tang et al. (2003), a two-dimensional aerodynamic kernel function is used to calculate aerodynamic forces on discretized elements of the aerodynamic system (see Fig. 2). In the aerodynamic vortex-lattice discretization, the chord length is divided into km segments of length dx in the chordwise direction, the wake is divided into $kmm-km$ segments of length dx in the chordwise direction, and the panel width is divided into kn segments of length dy in the spanwise direction. In the analyses that follow, km is taken as 60, kmm is taken as 120, and kn is taken as 5. Horseshoe point vortices are placed at the quarter chord of each element while collocation points are placed at the three-quarter chord of each element. The collocation points require the total induced velocity to match the unsteady motion of the panel. This condition leads to the relationship:

$$w_i^{t+1} = \sum_j^{k_{mm}} K_{ij} \Gamma_j^{t+1}, i = 1, \ldots, k_m, \tag{1}$$

where w_i^{t+1} is the induced velocity at time step $t+1$ and collocation point i, the aerodynamic kernel is K_{ij}, and Γ_j is the strength of the jth vortex. The aerodynamic kernel can be expressed as

$$K_{ij} = \frac{-1}{4\pi(y_i - y_{ja})}\left[1 + \frac{\sqrt{(x_i - x_{ja})^2} + \sqrt{(y_i - y_{ja})^2}}{x_i - x_{ja}}\right] + \frac{1}{4\pi(y_i - y_{jb})}\left[1 + \frac{\sqrt{(x_i - x_{ja})^2} + \sqrt{(y_i - y_{jb})^2}}{x_i - x_{ja}}\right], \tag{2}$$

where the subscript i denotes the ith collocation point and quantities subscripted ja and jb refer to the location of the jth pair of trailing vortex lines in the chordwise direction (Katz and Plotkin, 2001). The kernel function is used to calculate influence coefficients on every element of the panel with respect to every other point on the panel. These influence coefficients can then be used in combination with the discretized vortex strengths to form the aerodynamic matrix equality relating vortex strengths to induced velocities throughout the aerodynamic system:

$$[A]\{\Gamma\}^{t+1} + [B]\{\Gamma\}^t = \{w\}^{t+1}, \tag{3}$$

where the superscript t refers to a given timestep, the superscript $t+1$ refers to the next timestep, and both $[A]$ and $[B]$ are matrices of influence coefficients governing the mutual interactions of the discrete vortex elements.

As implied by the theoretical formulation of Eq. (1), a linear relationship between induced velocity at the collocation points and modal panel displacement q and velocity $\dot{q}$ is assumed. By doing so, we can indirectly relate aerodynamic forces to out-of-plane deflection as

$$\{w\} = [E]\{\theta\}, \tag{4}$$

where $\{\theta\} = [q, \dot{q}]^T$ is a vector of panel coordinates (Tang et al., 2003). This out-of-plane deflection amplitude will be particularly important in predicting the power generated by self-excited panel oscillations. Combining Eqs. (3) and (4) gives the governing aerodynamic matrix equation for this system:

$$[A]\{\Gamma\}^{t+1} + [B]\{\Gamma\}^t - [E]\{\theta\}^{t+1} = 0. \tag{5}$$

Next, it is necessary to define the pressure distribution at every point on the panel such that a mathematical expression for the generalized force on each element can be derived. Such an expression for the normalized pressure distribution can be derived following Tang et al. (2003) as

$$\overline{\Delta p_j} = \frac{c}{dx}\left[\frac{(\Gamma_j^{t+1} + \Gamma_j^t)}{2} \sum_j^i (\Gamma_i^{t+1} - \Gamma_i^t)\right], \tag{6}$$

where $\overline{\Delta p_j}$ is normalized pressure and c is the chord length. The generalized aerodynamic force at each point Q_i can then be expressed as

$$Q_i = \rho_\infty U^2 \int_0^c \overline{\Delta p} \Phi_i \, dx, \tag{7}$$

where ρ_∞ is the downsteam fluid density, U is the fluid velocity. In Eq. (7), Φ_i is the ith downwash mode function:

$$\Phi_i = \begin{cases} 0 & \text{for } x \le L_0 \\ \phi_i & \text{for } L + L_0 \ge x \ge L_0 \end{cases}, \tag{8}$$

where ϕ_i is the ith structural bending mode function of a two-dimensional cantilevered flat plate.

For simplicity additional modal mass and stiffness due to piezoceramic laminates are presumed to have a negligible effect on the aeroelastic system dynamics. For a discussion on how the dynamic response of linear heterogeneous beams differ from that of a continuous beam, see the work of Stanton and Mann (in review). In this particular study, uniform beam theory provides a sufficient approximation to the true dynamics of the system. However, it is recognized that achieving the optimal design, a topic of future work, will require a more detailed representation of the partial piezoelectric coverage. A relevant discussion of this issue can be found in Erturk et al. (2009). Finally, to ensure numerical convergence a value of $\alpha = 0.992$ is used as the vortex relaxation factor in the computations (Tang et al., 2003).

2.2. Structural model

2.2.1. Definition of system energies

The kinetic energy T of the flapping flag can be written as

$$T = \frac{1}{2} m_p \int_0^L (\dot{u}^2 + \dot{w}^2)\, dx, \tag{9}$$

where u is in-plane deflection, w is out-of-plane deflection, and m_p is mass per unit length of the plate. The potential energy V can be expressed as

$$V = \frac{1}{2} \int_0^L D\psi''^2\, dx, \tag{10}$$

where D is the flexural rigidity of the panel and ψ'' represents the nonlinear curvature formulation utilized by Semler et al. (1994). By applying conservation of energy at the point at which all system energy is kinetic (i.e. after the beam has just restored itself to its undeflected state), one can define an approximate measure of power delivered to this system P as

$$P = \dot{T} + \dot{V} = \dot{T}_{\max}. \tag{11}$$

Essentially, Eq. (11) assumes that all of the power necessary to maintain energy transfer between kinetic and potential forms at the rate defined by the time required for the system to move from a zero kinetic energy state to a zero potential energy state is being delivered to the beam by the flow. While simple, it does give valuable information about the energy harvesting potential of this system. A more detailed discussion of energy transfer phenomena in cantilevered plates in axial flow can be found in the work of Tang et al. (2009). In a practical sense, to extract a measure of the power delivered to this system, one can approximate time derivatives by multiplying by the system oscillation frequency in radians per second, ω, such that Eq. (12) becomes a useful approximation of the power delivered, assuming negligible in-plane deflection. This conception of the derivative is valid under the assumption of simple harmonic motion at the dominant aeroelastic mode. It is then a simple matter to work out the approximate expression for fluid power delivered to the beam as presented below:

$$P = \dot{T}_{\max} \approx \frac{1}{2} m_p \omega \int_0^L (w\omega)^2\, dx. \tag{12}$$

The above expression will be particularly useful in estimating the efficiency of the system.

2.2.2. Nonlinear electroelastic equations of motion

Kinetic and potential energy formulations similar to those in Eqs. (9) and (10) can be applied to the oscillating plate in order to derive the equations of motion by Hamilton's principle (Tang et al., 2003; Stanton and Mann, in review). This study utilizes both the nonlinear uniform aeroelastic beam model of Tang et al. (2003) and the nonlinear electroelastic beam model of Stanton and Mann (in review). For a nonlinear beam undergoing moderately large amplitude motion, each of these analyses involves applying the inextensibility condition along the neutral bending axis (Da Silva and Glynn, 1978; Semler et al., 1994). The analyses in Tang et al. (2003) and Stanton and Mann (in review) detail two valid ways to approach this derivation that yield similar results. Both make the key assumptions that out-of-plane deflection is small and that mechanical bending stress in directions along both span and thickness is negligible. Combining the results of Tang et al. (2003) for a uniform cantilevered plate in axial flow with the electromechanical model of Stanton and Mann (in review) for a cantilevered beam augmented with a piezoelectric bimorph under arbitrary forcing (with piezoelectric nonlinearities neglected for simplicity) gives the following system of coupled nonlinear ordinary differential equations:

$$M_{ii}\ddot{q} + \sum_n \sum_r \sum_s M_{inrs} q_n q_r \ddot{q}_s + \omega_i^2 M_{ii} q_i + F_K + F_M - \Theta_i v = Q_i, \tag{13a}$$

$$C\dot{v} + \frac{1}{R} v + \Theta_i \dot{q}_i = 0, \tag{13b}$$

where q_i is the modal panel displacement attributable to the ith structural mode normalized by L, v is absolute voltage across the electrical load, M_{ii} is an element of the mass matrix, F_K is a nonlinear force resultant from the curvature of the cantilevered plate, F_M and $\sum_n \sum_r \sum_s M_{inrs} q_n q_r \ddot{q}_s$ are nonlinear inertial forces, and ω_i is a modal natural frequency of the panel. In the electrical network equation, Θ_i is an element of the modal electromechanical coupling vector, C is the effective capacitance of the series-connected piezoelectric laminates, and R is effective resistance of the electrical system. The appropriate expressions for inertial, damping, and stiffness terms are given as

$$M_{ii} = \int_0^1 m_p \phi_i^2\, dx, \tag{14a}$$

$$F_M = \sum_n \sum_r \sum_s M_{inrs} q_n \dot{q}_r \dot{q}_s, \tag{14b}$$

$$F_K = \sum_n \sum_r \sum_s K_{inrs} q_n q_r q_s, \tag{14c}$$

$$K_{inrs} = \int_0^1 D\phi_i[\phi_n'''' \phi_r' \phi_s' + 4\phi_n' \phi''_r \phi_s''' + \phi''_n \phi''_r \phi''_s]\, dx, \tag{14d}$$

and

$$M_{inrs} = \int_0^1 m_p \phi_i \phi_n' \left(\int_0^x \phi_r' \phi_s' \, dx \right) dx - \int_0^1 m_p \phi_i \phi''_n \left(\int_x^1 \int_0^x \phi_r' + \phi_s' \, dx \, dx \right) dx, \tag{14e}$$

where D is taken as flexural rigidity and m_p is taken as the mass per unit chord length of the plate (Tang et al., 2003). The expressions for the equivalent capacitance of the piezoelectric bimorph and electromechanical coupling vector are, respectively,

$$C = \frac{\varepsilon_{33} b_p L_p}{2h_p}, \tag{15a}$$

$$\Theta_i = \frac{1}{2} e_{31} b_p (h_p + h) \phi_i'(L_p), \tag{15b}$$

where ε_{33} and e_{31}, respectively, denote the permittivity and electromechanical coupling factor of the piezoelectric material, h_p is the piezoelectric transducer thickness, b_p is the width of the piezoelectric section, L_p is length of the piezoelectric segment, and h is the thickness of the plate (Stanton and Mann, in review).

The above formulation requires several important assumptions. Note, for example, that the piezoelectric transducer is assumed to be placed at the root of the plate and that a passive load is assumed when calculating equivalent system capacitance. Similarly the plate is assumed to be of uniform density such that m_p is constant. Nonlinear terms in the electromechanical coupling are also neglected, an action that is adequately justified by comparison to experiment in a later section (Stanton and Mann, 2010; Stanton et al., 2010a,b). Finally, the nonlinear inertia term of Eq. (14e) will be neglected for computational efficiency. Previous studies have shown that neglecting this term does not significantly effect theoretical predictions (Tang et al., 2003).

2.3. Aeroelectroelastic state space equations

Numerical solutions for discrete time histories $q(t)$ and $v(t)$ and the use of linear eigenvalue methods to determine flutter characteristics is accomplished by transforming Eqs. (13a) and (13b) into a single discrete equation in state space. The first step of this transformation involves writing the governing equations in state space form:

$$\begin{bmatrix} M_{ii} & 0 & 0 & 0 \\ 0 & 1 & 0 & 0 \\ 0 & 0 & 0 & 0 \\ 0 & 0 & 0 & 1 \end{bmatrix} \begin{Bmatrix} \ddot{q} \\ \dot{q} \\ \ddot{v} \\ \dot{v} \end{Bmatrix} + \begin{bmatrix} 0 & \omega^2 M_{ii} & 0 & -\Theta_i \\ -1 & 0 & 0 & 0 \\ \Theta_j & 0 & C & \frac{1}{R} \\ 0 & 0 & -1 & 0 \end{bmatrix} \begin{Bmatrix} \dot{q} \\ q \\ \dot{v} \\ v \end{Bmatrix} = \begin{Bmatrix} Q_i - F_N \\ 0 \\ 0 \\ 0 \end{Bmatrix}, \tag{16}$$

where F_N, the normalized nonlinear force, is defined as in Tang et al. (2003):

$$F_N = \frac{F_K}{\tau^2} + \frac{F_M}{m_p L^2}. \tag{17}$$

Discretization of Eq. (16) is accomplished by applying the following temporal differencing schemes to appropriate terms involving both q and v, taking Δt as the timestep and x as a general coordinate:

$$x_i = \frac{x^{t+1} + x^t}{2}, \tag{18a}$$

$$\dot{x}_i = \frac{x^{t+1} - x^t}{\Delta t}, \tag{18b}$$

$$\ddot{x}_i = \frac{\dot{x}^{t+1} - \dot{x}^t}{\Delta t}. \tag{18c}$$

Substituting the discretized forms of both the panel response $\{\theta\}$ and the voltage vector $\{v\}$ and subsequently solving for two new coefficient matrices allows one to re-express Eq. (16) as

$$\begin{bmatrix} D_2 & H_2 \\ J_2 & K_2 \end{bmatrix} \begin{Bmatrix} \theta \\ v \end{Bmatrix}^{t+1} + \begin{bmatrix} D_1 & H_1 \\ J_1 & K_1 \end{bmatrix} \begin{Bmatrix} \theta \\ v \end{Bmatrix}^{t} = \begin{Bmatrix} Q_i - F_N \\ 0 \end{Bmatrix}^{t+(1/2)}, \tag{19}$$

where $[D_1]$, $[D_2]$, $[H_1]$, $[H_2]$, $[J_1]$, $[J_2]$, $[K_1]$, and $[K_2]$ are compact expressions for the four quadrants of the new coefficient matrices. To obtain a full state space representation of the aeroelectroelastic system, however, it is necessary to integrate the aerodynamics derived earlier into this structural model (Tang et al., 2003). The first step in accomplishing this is by re-writing the aerodynamic force Q_i, in light of Eqs. (6) and (7) from the vortex-lattice formulation, in a temporally discretized form:

$$-Q_i = [C_2]\{\Gamma\}^{t+1} + [C_1]\{\Gamma\}^t. \tag{20}$$

This leads to the re-expression of Eq. (19) in augmented form as

$$\begin{bmatrix} 0 & 0 & 0 \\ C_2 & D_2 & H_2 \\ 0 & J_2 & K_2 \end{bmatrix} \begin{Bmatrix} \Gamma \\ \theta \\ \nu \end{Bmatrix}^{t+1} + \begin{bmatrix} 0 & 0 & 0 \\ C_1 & D_1 & H_1 \\ 0 & J_1 & K_1 \end{bmatrix} \begin{Bmatrix} \Gamma \\ \theta \\ \nu \end{Bmatrix}^{t} = \begin{Bmatrix} 0 \\ -F_N \\ 0 \end{Bmatrix}^{t+(1/2)}. \tag{21}$$

Finally, replacing the trivial first row of Eq. (21) with the aerodynamic matrix equality of Eq. (5) gives the complete aeroelectroelastic state space model:

$$\begin{bmatrix} A & -E & 0 \\ C_2 & D_2 & H_2 \\ 0 & J_2 & K_2 \end{bmatrix} \begin{Bmatrix} \Gamma \\ \theta \\ \nu \end{Bmatrix}^{t+1} + \begin{bmatrix} B & 0 & 0 \\ C_1 & D_1 & H_1 \\ 0 & J_1 & K_1 \end{bmatrix} \begin{Bmatrix} \Gamma \\ \theta \\ \nu \end{Bmatrix}^{t} = \begin{Bmatrix} 0 \\ -F_N \\ 0 \end{Bmatrix}^{t+(1/2)}. \tag{22}$$

Eq. (22) fully incorporates the aerodynamic, mechanical, and electrical aspects of the flapping flag energy harvester into a single nonlinear aeroelectroelastic state space expression. This simplicity of this discrete expression makes it particularly useful for application to computational simulation of system behavior.

3. Experimental system

The experimental system was designed to emulate the theoretical aeroelectroelastic system as closely as possible. A rigid airfoil clamping device was constructed from two symmetric metal pieces connected through the thickness by two sets of ten screws. The airfoil itself was formed in the shape of a standard NACA 0015 section while its ends were attached to the top and bottom of the wind tunnel. The 2024-T6 aluminum elastic plate was mounted between the two halves of the metal airfoil at the center of the airfoil span with a length L_0 being internal to the airfoil, leaving a reduced beam length L actually exposed to the flow. An airfoil was used to clamp the cantilevered beam in order to ensure smooth flow along the beam that would allow for the isolation of aeroelastic damping phenomena.

Linear axial strain gauges were used to extract frequency and root strain data. An adhesive (M-bond 200) was used to securely bond a pre-wired linear strain gauge (OMEGA) to the root of the plate at the lowest extent of the span on each side of the plate. The output of these strain gauges was combined to form a classical Wheatstone bridge with an 8 V excitation potential. The measured voltage across this bridge was recorded in 4 s increments using a data acquisition box linked to custom software (Labview). These voltage signals could then be utilized to calculate experimental time histories for absolute root strain.

To allow for electrical transduction, piezoelectric patches (MIDE Quickpack QP10w) were mounted as close as possible to the root of the plate in the center of the spanwise direction of the plate with a generically available epoxy. Pre-manufactured four-pin connectors were detached from the thin film leads, which were then soldered to conventional wiring. These wires were arranged such that the piezoelectric patches were connected in series both with each other and with a variable resistor box. Voltage across this variable resistor box was recorded using the aforementioned data acquisition setup. Material properties of the airfoil, elastic plate, and piezoelectric patches can be found below in Table 1.

A digital camera and strobotac were also mounted on the top surface of the wind tunnel to allow for effective and standardized measurement of panel response amplitude. The strobotac was used to artificially lower the frequency observed by the digital camera such that each individual frame would contain only a single image of the plate, making such frames more suitable for handling by image processing software. The digital camera was used to record movies of several seconds in duration that would allow for the determination of maximum amplitude by means of custom image processing software which extracts and analyzes appropriate video frames. Finally, mean wind tunnel flow velocity was measured with a conventional Pitot tube and confirmed by simultaneous measurement with a hot wire.

3.1. Experimental procedures

The first experimental procedure was to increase wind tunnel speed rapidly until it was just below the predicted linear flutter speed. From here, the wind speed was slowly increased in increments of approximately 0.5 m/s. Strain and voltage measurements were taken at each increment. This slow increase continued until the onset of large amplitude LCO, at which point the wind speed was decreased by approximately 0.5 m/s with strain and voltage data again being taken at every point until LCO ceased at the low extreme of the hysteresis band.

The second experimental procedure was designed primarily to measure LCO amplitude, but was also useful for confirming the accuracy of the frequencies obtained from performing a Fast Fourier Transform (FFT) on the root strain signals. In this scenario, ambient lighting was extinguished and wind speed was again quickly increased to just below the predicted linear flutter speed. Wind speed was slowly increased up to LCO onset, stopping at the exact same flow velocities

Table 1
Experimental parameters.

Parameter	Symbol	Value
Rigid airfoil properties		
Span	s	550 mm
Chord	L_0	101 mm
Elastic plate properties		
Total length	L_T	386 mm
External length	L	310 mm
Width	b	101 mm
Thickness	h_s	0.39 mm
Density	ρ_s	2840 kg/m^3
Young's modulus	E_s	72.4 GPa
Poisson's ratio	ν_s	0.33
Damping ratio	D_s	0.005
Piezoelectric laminate properties		
Length	L_p	25.4 mm
Width	b_p	20.3 mm
Thickness	h_p	0.25 mm
Density	ρ_p	7500 kg/m^3
Young's modulus	E_p	67 GPa
Poisson's ratio	ν_p	0.31
Coupling coefficient	e_{31}	-16.6 C/m^2
Laminate permittivity	ε_{33}	25.5×10^{-9} F/m

used in the first procedure. These velocities were again confirmed both with a hot wire and with a conventional Pitot tube. At each point, several seconds of video were taken with a digital camera while the strobotac provided necessary light at a frequency slightly below the theoretical LCO frequency. Once LCO onset occurred, this same procedure was implemented while flow velocity was decreased through the hysteresis band until LCO amplitude went to zero. At each point, the strobotac frequency was modulated in order to exactly match the frequency of LCO oscillation, allowing for a direct measurement that could be utilized to confirm the accuracy of the FFT of the analogous root strain signal. As would be expected, these two sets of frequency results were generally in close agreement.

A final experiment performed using this model was accomplished by increasing wind speed quickly until LCO onset occurred and then lowering it back down to a speed slightly above that at which LCO amplitude went to zero. While physical LCO amplitude was not maximized at such a speed, the fact that the oscillations were also much less violent facilitated observation of whether or not the electrodynamics of the system could affect its physical dynamics. Once the test wind speed was attained, the resistance of the variable resistor box was modulated among a spectrum of values while voltage and strain data were taken at each resistance value. This procedure allows for the extraction of an experimental power versus resistance, or *P–R*, curve that will give some insight as to how the passive load on this system can be best optimized for capturing electrical power. An analogous amplitude measurement with varying resistance was not undertaken due to the fact that initial investigations revealed very little change in LCO amplitude as a result of changing resistance within even a very wide range. It is possible that with a more substantial piezoelectric transducer, changes in the electrical network could indeed have a significant impact on physical oscillation of the system.

3.2. Data analysis

Strain gauge voltage data was converted to root strain using the widely known transformation characteristic of a Wheatstone bridge. A sample strain signal can be found in Fig. 3. An FFT procedure was also performed on the root strain signal to determine the dominant frequencies of oscillation. Piezoelectric voltage data was processed by finding the maximum amplitude of the voltage signal and using knowledge of the resistance value to calculate power received by the load. Root mean square (rms) voltage was calculated under the simplifying assumption that the voltage signals are purely harmonic. Frequency data from the strobotac procedure needed no further processing. The bulk of the data processing procedures were targeted toward determining experimental LCO amplitude. At each wind speed, MATLAB was used to extract two frames from the corresponding video. One of these frames showed the panel completely straight while the other showed the panel at maximum deflection. It was then possible to determine the chord length in pixels for a particular image by finding the distance between the root of the beam and the end of the beam while determining the amplitude in pixels in a similar fashion. The amplitude pixel measurement was then divided by the chord pixel measurement to determine a chord normalized amplitude at each wind speed. A sample image processing frame in which the two images specified above are superimposed for ease of analysis can be found in Fig. 4.

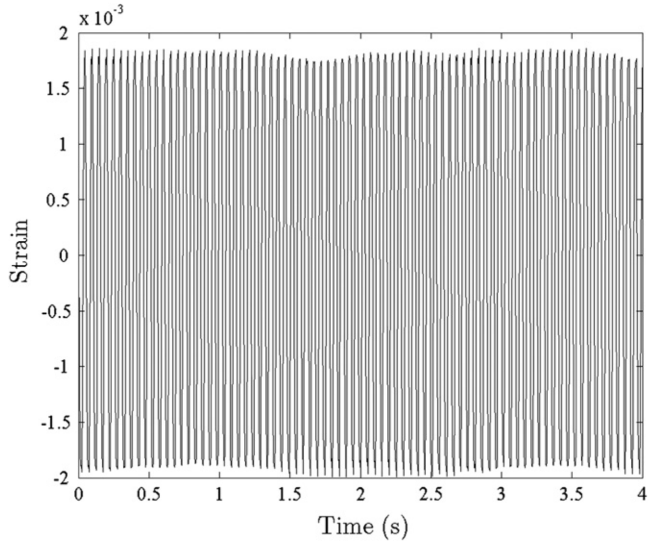

Fig. 3. Sample time history of an experimental strain signal at 28.6 m/s flow speed.

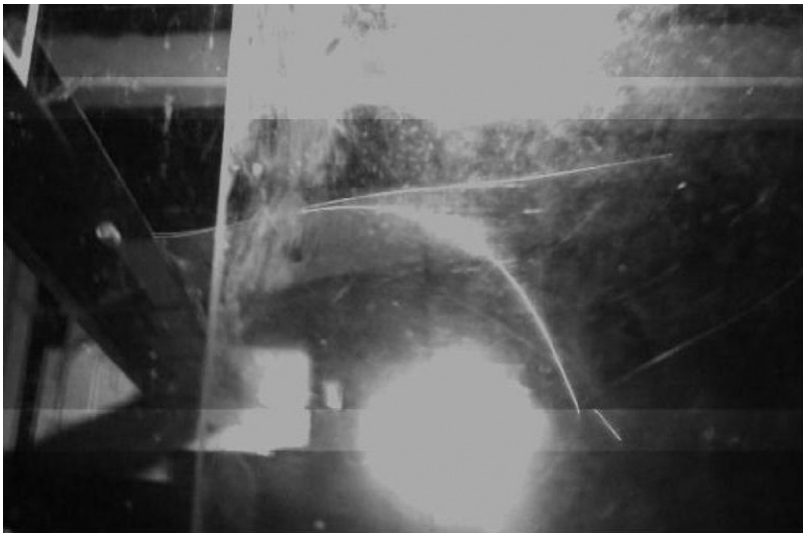

Fig. 4. Sample superposition frame of chord and maximum deflection images.

4. Experimental and theoretical results

Prior to the wind tunnel experiment, the natural frequencies of the cantilevered beam were measured with and without the piezoelectric transducer attached. This was accomplished by connecting the strain gauge at the root of the beam to a dynamic FFT analyzer. Before transducer attachment, natural frequencies of 3.50, 19.75, 57.50, and 116 Hz were measured. These results are in relatively good agreement with values of 3.46, 22.0, 61.5, and 119 Hz predicted by classical beam theory. After attachment of the piezoelectric transducer, open circuit natural frequencies of 3.88, 21.1, 60.0, and 118 Hz were measured. These are again in relatively good agreement with values of 3.91, 24.2, 67.0, and 129 Hz predicted by discontinuous piezoelectric beam theory (Stanton and Mann, in review). The slight deviation between theory and experiment in natural frequencies at higher modes is unexpected, but given that the first and second modes are known to govern the phenomenon in question, these higher modes should not significantly affect the beam LCO motion. The experimental natural frequencies were directly input into the theoretical model to closely emulate the experimental system. While the fourth mode in particular does not have a great deal of influence on the physical behavior of the system, it was included for the sake of completeness.

4.1. Characterization of limit cycle oscillations

4.1.1. Flutter boundary determination

One of the most important theoretical characteristics of this system is the flow speed at which the real eigenvalues corresponding to negative system damping first become positive. At this point, known as the linear flutter speed, the system becomes unstable and will enter LCO when sufficiently displaced from its rest state. Fig. 5 shows a sample theoretical displacement time history in which such large amplitude LCO can be observed. A theoretical methodology based on linear eigenvalue analysis was applied to calculate the linear flutter speed from the aeroelectroelastic state space matrices of Eq. (22). Specifically, this method involves calculating the eigenvalues of the aeroelectroelastic system at different flow velocities within an appropriate range and mathematically solving for the velocity at which the real part of these eigenvalues (i.e. the negative system damping) first becomes positive. Fig. 6(a) shows in detail how the various eigenvalue branches evolve with changes in flow velocity while Fig. 6(b), a root locus plot of the aeroelectroelastic system, indicates that the eigenvalue branch associated with the second aeroelastic mode (with an oscillation frequency near 20 Hz) is in fact the one that drives the system to instability. This conclusion is quite similar to that drawn from the work of Tang et al. (2003). The real eigenvalue branch associated with this mode, denoted by squares in Fig. 6(a), crosses zero

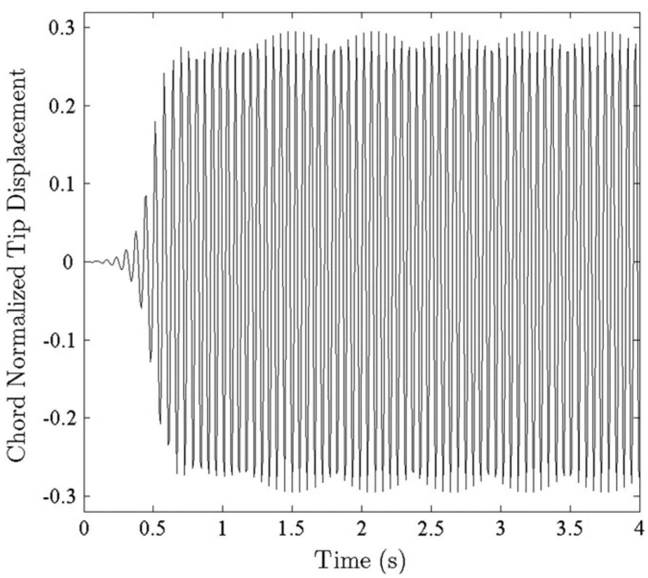

Fig. 5. Sample theoretical time history at 35 m/s.

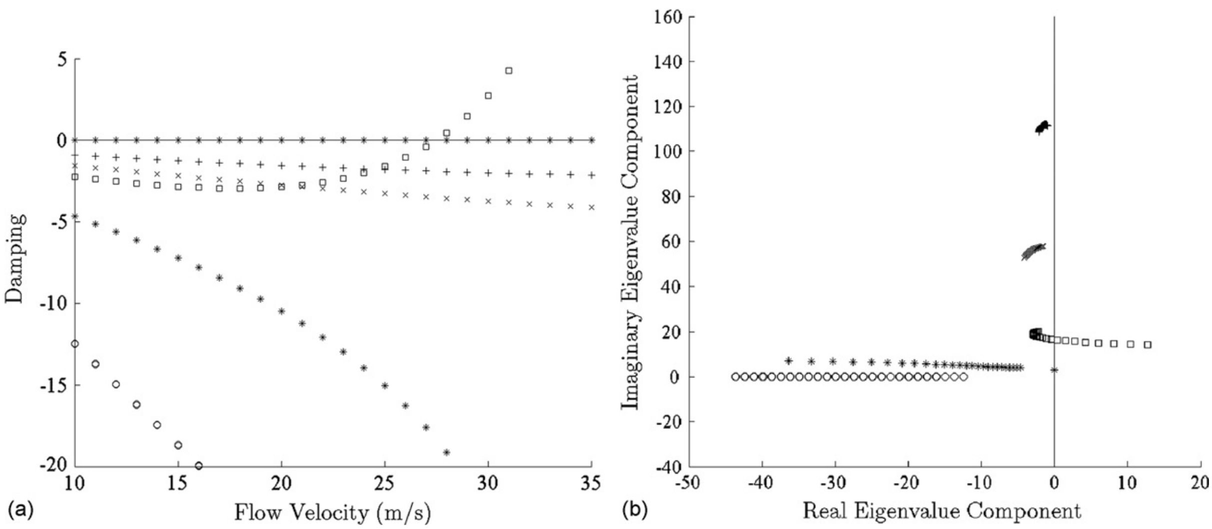

Fig. 6. Eigenvalue method for flutter speed determination: (a) Damping versus flow velocity and (b) Root-locus of aeroelectroelastic system.

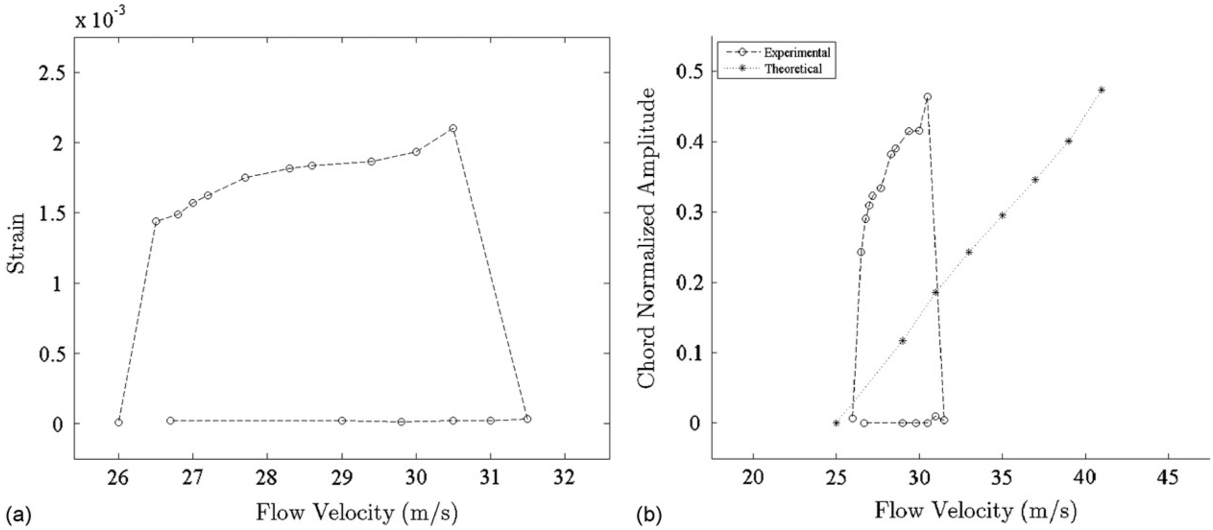

Fig. 7. Experimental and theoretical amplitude measures: (a) Root strain amplitude versus flow velocity and (b) Normalized amplitude versus flow velocity.

at a flow speed of approximately 28 m/s. It is interesting to note as well a stagnant real eigenvalue branch directly attributable to the piezoelectric transducer that always takes a value of zero. This branch seems to be associated with an oscillation frequency (i.e. an imaginary eigenvalue) equivalent to that of the first structural mode. Unlike the aeroelastic modes, which do slightly change frequency as velocity changes, this electrostructural mode appears to be completely stagnant both in terms of limited stability and first mode oscillatory characteristics.

The simplest way to determine the degree to which these theoretical results are validated by experiment is to compare the predicted flutter speed to the wind speed at which the onset of LCO is observed in practice. At this velocity, the real negative damping eigenvalues become positive and the plate begins to oscillate with large amplitude because structural damping can no longer completely counteract negative aerodynamic damping. The plot of root strain amplitude versus flow velocity in Fig. 7(a) clearly shows the dramatic root strain increase indicative of LCO onset at 31.5 m/s. While this experimental flutter speed is not exactly the same as the theoretical value of 28 m/s, it is certainly within reasonable bounds. A similar trend can be observed in the LCO amplitude plot of Fig. 7(b), which confirms this finding.

Another crucial criterion for evaluating the efficacy of the theoretical model is how well the particular LCO characteristic of this system are predicted. While the system should theoretically experience self-excited LCO at and above the linear flutter speed, it is also possible that, once excited, LCO will in fact be sustained at speeds below the linear flutter speed. These large amplitude oscillations below the linear flutter speed are generally termed "subcritical" LCO. Experimentally, as shown in Figs. 7(a) and (b), subcritical LCO are observed from 31.5 down to 26 m/s. The amplitude of these subcritical LCO appears to vary nonlinearly with air speed. There is thus a distinct contrast between the theoretical prediction that supercritical LCO should start at 28 m/s and increase in amplitude with flow velocity and the experimental observation of large amplitude subcritical LCO beginning exactly at the experimental flutter speed. This finding confirms those of Tang et al. (2003) concerning a significant subcritical hysteresis band not predicted by nonlinear theory. Additional work on understanding the source of this discrepancy is currently being undertaken, particularly with regards to understanding the significant effect that a small rectangular duct such as a wind tunnel can have on the pressure oscillations of such a system (Rosenhead, 1930; Doaré et al., 2011). A particularly promising approach used to model related systems in enclosed spaces can be found in the work of Howell et al. (2009). Nonetheless, while the nature of the theoretical and experimental limit cycles seems to differ, there is still distinct value in analyzing how well various system quantities are predicted in terms of oscillation amplitude, whether the oscillations themselves are supercritical or subcritical. Moreover, the model's accurate prediction of linear flutter speed and trends in amplitude with increasing flow velocity seems to adequately validate the predictive power of the theoretical model and to confirm the accuracy of the aeroelectroelastic formulation presented earlier within this manuscript.

4.1.2. *Amplitude measures*

One of the most important aspects of this system is the particularly high amplitudes of its characteristic self-excited limit cycles. The plot of amplitude normalized by chord versus flow velocity in Fig. 7(b) indicates that normalized amplitudes ranging from 0.00 to 0.46 were observed experimentally within 5 m/s of the flutter boundary, with the maximum amplitude occurring exactly at the flutter boundary. Increasing the wind speed above the flutter boundary also increased the LCO amplitude further, but for safety reasons experiments were focused on speeds at and below the flutter boundary. As is also apparent from this figure, there is a nonlinear relationship between flow velocity and normalized amplitude that causes a mild drop in amplitude with velocity just below the flutter speed that become much sharper as velocity (and amplitude itself) decreases. Note also the close similarity in form between the pattern of data points in Figs. 7(a) and (b), which seems to imply that root strain could in fact be used as a valid proxy for amplitude if an appropriate linear transformation were to be applied. Such a procedure could be of use in future experiments where a large number of data points would make the image processing algorithm currently used to find experimental amplitude too laborious.

4.1.3. Frequency measures

The final significant characteristic of these LCO is their dominant frequency of oscillation. Experimental oscillation frequencies at all flow velocities from both strobotac and root strain FFT procedures were nearly identical. Theoretical oscillation frequencies were found by calculating a time history at each wind speed and performing the same FFT procedure on the theoretical time history that was used to transform the strain signal. A sample FFT of the root strain signal can be found in Fig. 8(a) while a sample FFT of the theoretical time history can be found in Fig. 8(b). The calculated theoretical frequencies in Fig. 8(c) are quite similar to the experimental ones (with a maximum deviation of under 10%) and, perhaps more importantly, they accurately match the trends of LCO frequency with velocity and amplitude. The high frequency, yet low intensity mode found in the experimental FFT signal of Fig. 8(a) in addition to the dominant response is most likely a result of extraneous (perhaps electrical) experimental system excitation, and thus the absence of a similar peak in the companion theoretical FFT signal of Fig. 8(b) is not unexpected. For the sake of visual convenience, system quantities from this point forward will be plotted versus normalized amplitude instead of flow velocity. Not only does this allow for a more useful comparison, but in the context of energy harvesting it is far more important to understand how the various characteristics of the system change with oscillation amplitude as opposed to flow velocities particular to this specific experimental system.

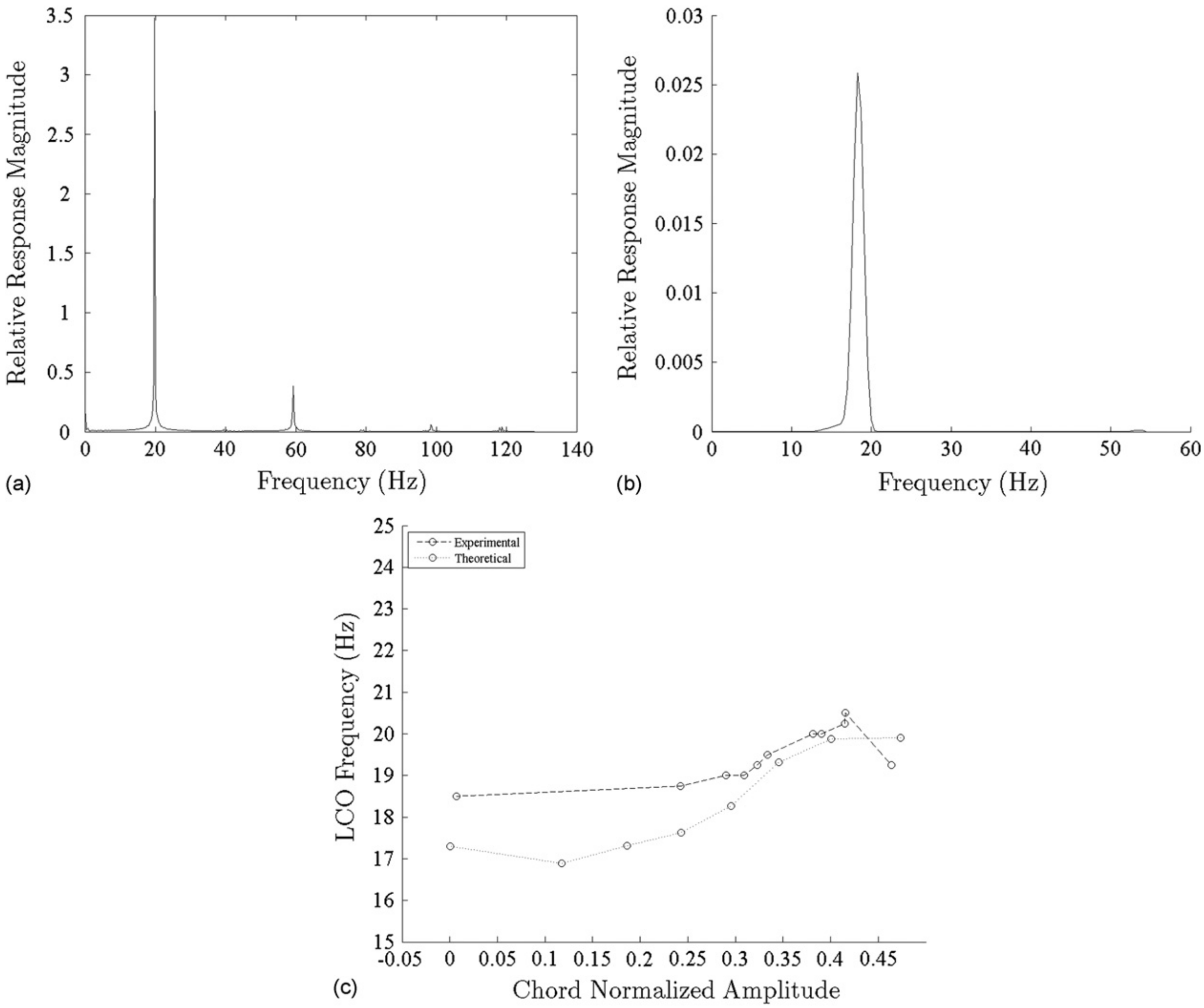

Fig. 8. Experimental and theoretical frequency measures: (a) FFT of experimental root strain signal, (b) FFT of theoretical time history and (c) LCO frequency versus normalized amplitude.

4.2. Electrical response to system excitation

4.2.1. Amplitude response

The most practical aspect of any harvester is the amount of power it can potentially produce. As such, the electrical response of this system is of significant interest. With resistance kept constant at 100 kΩ, the maximum voltage amplitude obtained from the piezoelectric patch was 11.25 V at 31 m/s, which corresponds to delivered rms power of just under 1 mW. Fig. 9(a) demonstrates how the amplitude of the voltage signal from the energy harvester varied with physical amplitude while Fig. 9(b) shows the analogous variation in power delivered to the load with physical amplitude. Both figures also include the theoretical prediction of the aeroelectroelastic state space model. The close agreement between experiment and theory observed in these figures implies that the electrodynamic addenda to the classical aeroelastic state space model were accurately formulated. The usefulness of a theoretical model that can quickly and accurately predict power output based on experimental amplitudes should not be understated. The relationship between power delivered and amplitude is predictably nonlinear given the quadratic variation of power delivered with voltage. Sample and theoretical voltage time histories can also be found in Figs. 10(a) and (b), respectively.

One particularly interesting aspect of these results is the distinctly linear form of the voltage amplitude versus amplitude normalized by chord data presented in Fig. 9(a). While piezoelectric transducers are by no means linear devices (Stanton and Mann, in review), the variation of voltage amplitude with physical amplitude in this system does seem to be of strikingly linear character. To further investigate this trend, voltage amplitude was regressed on amplitude normalized

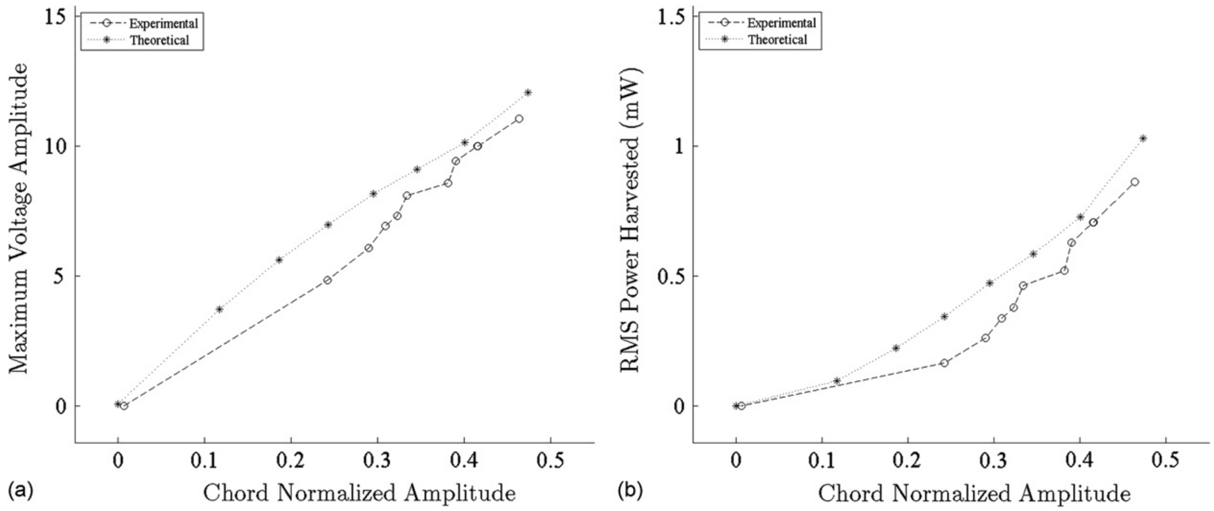

Fig. 9. Experimental and theoretical electrical response measures: (a) Experimental and theoretical voltage versus normalized amplitude and (b) Experimental and theoretical power versus normalized amplitude.

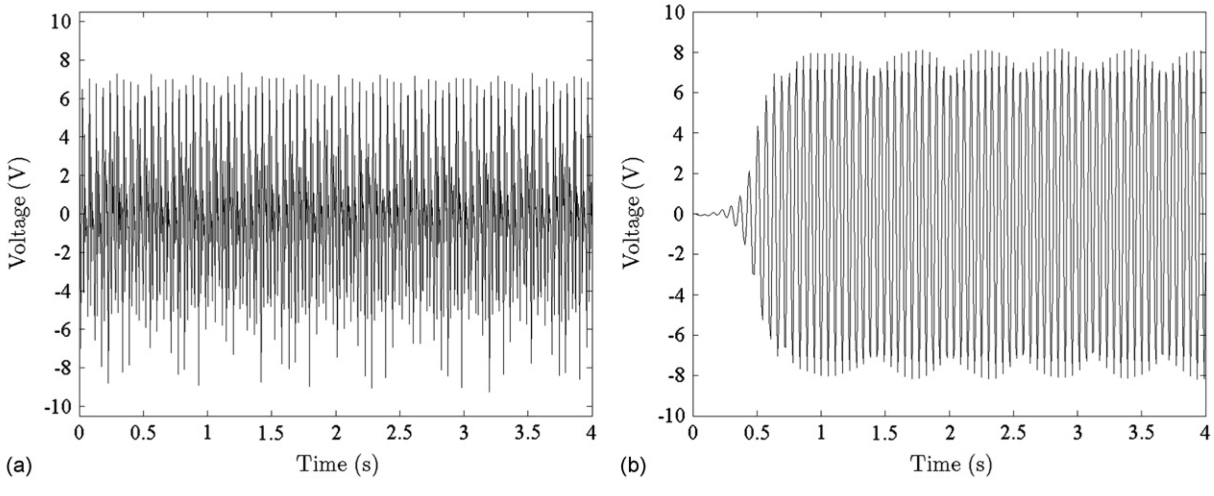

Fig. 10. Voltage time histories: (a) Sample experimental voltage time history and (b) Sample theoretical voltage time history.

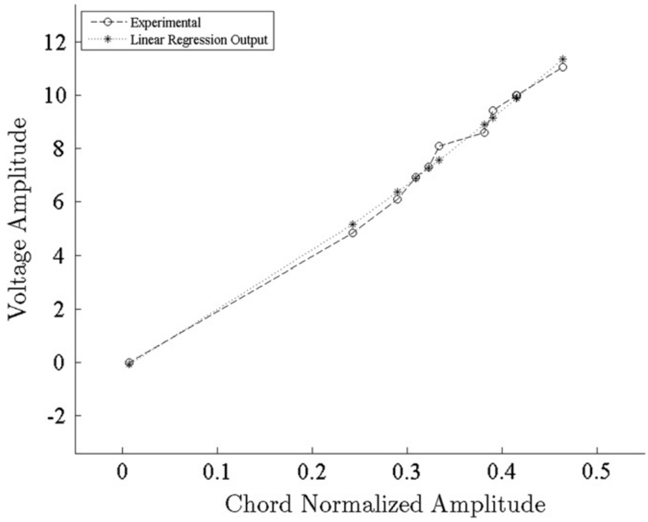

Fig. 11. Regression analysis of experimental piezoelectric linearity.

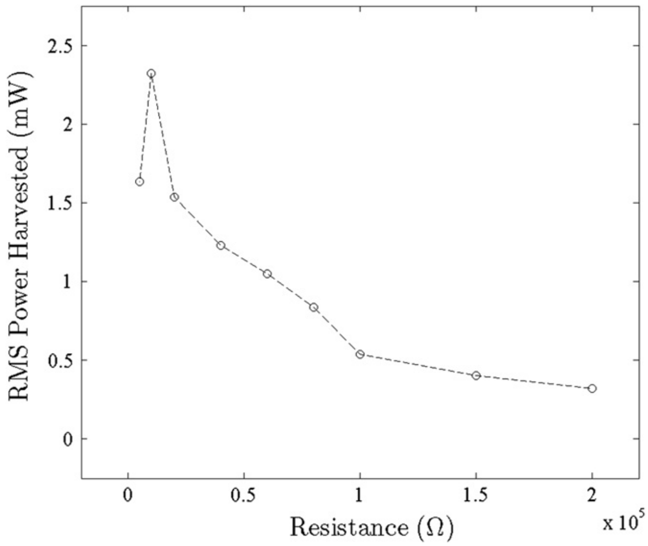

Fig. 12. Power versus resistance curve of energy harvester at 27 m/s.

by chord to determine the degree of linearity characteristic of the relation between these two variables. After a basic linear regression was performed, the coefficient of correlation between these two variables was calculated to be in excess of 0.99, clearly indicating that the relationship between physical and electrical amplitudes is primarily linear. Fig. 11 graphically illustrates the goodness of fit by simultaneously displaying the experimental voltage amplitude and regression predicted voltage amplitude versus normalized physical amplitude. These two series appear nearly identical. Such a result, significantly, would seem to justify the aforementioned neglect of the nonlinear piezoelectric coupling term in the formulation of Eqs. (13a) and (13b) when modeling this particular aeroelastic energy harvester. It is distinctly possible, however, that piezoelectric nonlinearity could become more pronounced in a system with stronger electromechanical coupling (Stanton and Mann, in review).

4.2.2. Load response

To round out the investigation of the energy harvesting potential of this system, it is necessary to understand how power delivered varies with circuit load magnitude. Optimizing this generally nonlinear relationship can often be crucial in obtaining useful amounts of electrical power from a given device. As described above, voltage measurements were recorded at several different resistance values at a constant wind speed of 27 m/s, a comparatively low amplitude state with a chord normalized displacement of 0.33 approximately 4.5 m/s below the experimental flutter boundary. Even at this relatively low velocity, as shown in Fig. 12, it was possible to extract just under 2.5 mW of rms electrical power at a resistance value of 10 kΩ. Even though the voltage amplitude at this resistance is lower than it was at 100 kΩ, the system power output nonetheless increases due to the order of magnitude decrease in resistive load. Optimizing the circuit load at other wind speeds should lead to analogous increases in power generated.

5. Efficiency calculations

As with any energy harvesting system, it is useful to obtain metrics on how efficiently power is being extracted from the environment. In this case, there are two appropriate measures: transduction efficiency and capture efficiency. Transduction efficiency defines how well the electrical system is able to access the energy of the oscillating plate segment to which it is coupled. The kinetic energy of the beam at a particular flow velocity was calculated using Eq. (12), taking q to be defined as the second physical (i.e. non-normalized) structural modeshape, ϕ_{2P}, that experiment and theory have shown to dominate the LCO of this system. The expression for ϕ_{2P} at a given flow velocity was explicitly calculated by constructing the normalized structural modeshape ϕ_2 from classical plate theory and appropriately transforming this expression to reflect physical displacements. The expression for this transformation can be found below, taking L as the length of the plate, $\tilde{q}_{\max}$ as the maximum experimental normalized tip displacement at a particular flow velocity and ϕ^{tip} as the maximum tip displacement of the appropriate normalized modeshape:

$$\phi_{2P} = \frac{\tilde{q}_{\max}}{\phi^{\text{tip}}} L \phi_2. \tag{23}$$

Using the above expression in place of the q term in Eq. (12) yielded a value for power delivered to the beam of 39.2 W at 27 m/s, the speed at which the load optimized rms power measurement of 2.5 mW was recorded. To obtain an approximate transduction efficiency using this load optimized rms power measurement, it is assumed that the power delivered to the beam is distributed equally throughout the area of the beam. It is then a simple matter to calculate a transduction efficiency μ_P using the following equation, taking P_P as the power output by the transducer, A_P as the area of the transducer, P_B as the power delivered to the beam, and A_B as the area of the beam:

$$\mu_P \approx \frac{P_P A_B}{P_B A_P}. \tag{24}$$

This method yields a transduction efficiency value of $\mu_P = 0.38\%$. There are a number of potential reasons for this relatively low value. First, due to experimental considerations involving pre-manufactured leads on the piezoelectric patch, it was necessary to place the base of the piezoelectric patch approximately an inch from the root of the beam. This was done in order to ensure that the entire patch would be attached to the beam instead of having the electrical leads spanning both the flapping flag and rigid airfoil. Were the electrical leads attached to the rigid airfoil, there is a distinct possibility that they would not have survived the violence of the LCO observed in this experiment. Interference with the smoothness of airflow caused by protrusions on the airfoil would also have been experimentally undesirable (Dowell, 2004). The construction of the rigid airfoil was also prohibitive to placing the base of the piezoelectric inside the airfoil itself. In addition to undergoing significant rigid body motion as a result of this placement, in contrast with the straining that would be desired of such a device, it would appear that the piezoelectric patch was co-located with a node of the second structural mode, a mode that is dominant in the observed LCO. That is, it seems that the patch was placed over a point at which the sign of the beam curvature changed, which itself would cause voltage cancellation in the piezoelectric (Erturk et al., 2009). These issues were almost certainly the reasons that this transduction efficiency was lower than expected, and should definitely be taken into account in later designs of aeroelastic energy harvesters. This efficiency can certainly be improved by optimizing the construction and placement of the piezoelectric transducer.

The true measure of how well this system performs as an energy harvester, however, is the percentage of the power in the flow accessed by the beam. The power in the flow P_F at a given wind speed can be easily calculated by the following classical equation, taking ρ as fluid density, V as flow velocity, and A as the cross sectional area under consideration:

$$P_F = \frac{1}{2}\rho V^3 A. \tag{25}$$

Thus, calculating capture efficiency μ_C can be accomplished by means of the complete expression (26) below, which combines Eqs. (12), (23), and (25) to define this fundamental metric in terms of basic experimental and theoretical quantities. Note that A is taken as the area defined by the width of the plate multiplied by twice its maximum physical amplitude $q_{\max}$ at the appropriate flow speed, the theoretical cross sectional area within which this harvester operates:

$$\mu_C = \frac{P_B}{P_F} \approx \frac{\frac{1}{2} m_p \omega \int_0^L \left(\frac{\tilde{q}_{\max}}{\phi^{\text{tip}}} L \phi_2 \omega \right)^2 dx}{\rho V^3 (b q_{\max})}. \tag{26}$$

Applying Eq. (26) to the system under consideration gives a flow energy value of 235 W and a capture efficiency value of $\mu_C = 17.4\%$ at 27 m/s. It is also significant that the capture efficiency, as shown in Fig. 13, remains essentially constant as LCO amplitude (and wind speed) varies, meaning that, at least for a subcritical operating regime, similar efficiency should be observed over the entire velocity band of the energy harvester. While this 17% efficiency result may not seem

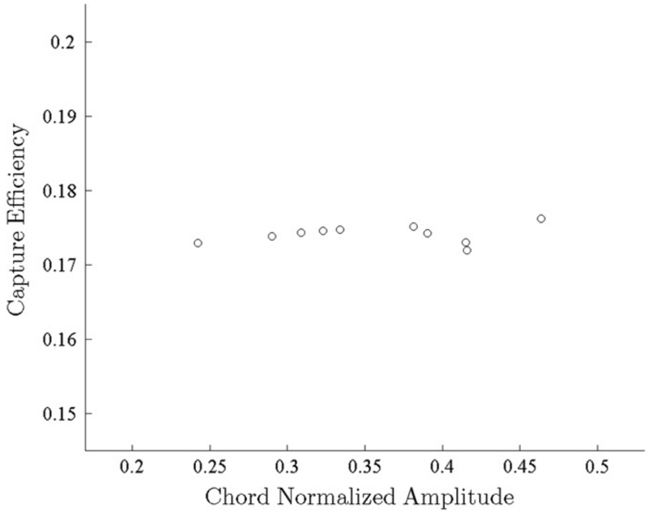

Fig. 13. Capture efficiency versus flow normalized amplitude.

particularly impressive in an absolute sense, it is important to evaluate this number in the greater context of wind turbine efficiency. Specifically, the classical Betz limit states that the maximum fraction of kinetic flow energy that can possibly be extracted from steady flow through an actuator disk of constant area is 59.3%. Moreover, even the most efficient modern wind turbines only capture around 35–45% of available flow energy, and to attain these capture efficiency values the freestream wind speed must generally be very close to the optimal operating speed of a given turbine. The fact that the rudimentary flutter generation concept demonstrated here has a capture efficiency of 17% over a relatively large velocity band is therefore quite significant in evaluating the potential utility of the flutter harvester concept.

The flow energy value of 235 W calculated above is also important in understanding these results in the context of previous work. In particular, Tang et al. (2009) theoretically predicted that a flutter harvester of slightly larger size than the one described here could capture on the order of 1 kW of power per meter length in a 40 m/s wind flow. When an analogous metric for this harvester is calculated from the 235 W power extraction value mentioned above and the 0.27 m exposed length of the cantilever, the value for this system comes out to approximately 870 W/m at a 27 m/s flow speed. This number is therefore in excellent agreement with the theoretical prediction of Tang et al. (2009), and is perhaps even more encouraging given that such a large amount of power per meter length was captured at a wind speed over 10 m/s below that for which Tang et al. (2009) evaluated their own theoretical prediction. Thus, the fact that this small rudimentary system is able to consistently access nearly a fifth of the significant amount of energy in the cross sectional area of its operation over a large velocity band reflects favorably on the prospect of harvesting useful amounts of power with devices designed to take advantage of the self-excited LCO of a flapping flag.

6. Summary and conclusion

A nonlinear state space model of an aeroelectroelastic system based on full three-dimensional vortex-lattice aerodynamics has been derived and implemented to predict crucial aspects of the behavior of an experimental aeroelastic energy harvester based on self-excited limit cycle oscillations of a flapping flag. Prediction of aeroelastic phenomena including LCO frequency and amplitude was similar to or superior to previous models of this type both in terms of quantitative prediction of experimental values and qualitative adherence to observed trends. It has also been shown that a linear electrostructural coupling term is more than adequate to model the interaction between the electrodynamics and structural dynamics of this particular iteration of the aeroelectroelastic flapping flag. While such a linear electroelastic formulation may prove adequate for many systems, the existence of electromechanical nonlinearity should nonetheless be considered in future applications. The experimental device itself has also been shown to have distinct energy harvesting potential at even low flow speeds that could be further enhanced to take advantage of extremely large LCO amplitudes by circuitry designed to enhance energy extraction from this dynamical system. The fact that nearly a fifth of the accessible flow energy was transferred to the plate even in this rudimentary design implies that aeroelastic energy harvesters designed to fully exploit large amplitude LCO could indeed access useful amounts of ambient environmental energy, particularly if optimized over relevant operating parameters.

Moreover, previous results in which experimental subcritical LCO were in contrast with supercritical LCO predicted by an aeroelastic state space model of the sort constructed here have been rigorously confirmed and replicated. It is distinctly possible that such a discrepancy between theory and experiment arises from the fact that self-excited LCO amplitudes in this system are so large that they are comparable to the length scale of the experimental test section of the wind tunnel. Pressure interactions with the wind tunnel boundaries might in such a case significantly affect the system dynamics to the point that it would be necessary to model the system as a flapping flag within a small duct in order to theoretically predict these large subcritical LCO. Theoretical work on this topic has already begun in an attempt to better understand this system and to more effectively predict its energy harvesting potential. Ultimately, it is quite promising that self-excited LCO of a small aeroelectroelastic beam are able to be sustained at amplitudes as large as those observed here, and the insight gained from continued efforts to model more accurately the aerodynamics of this system could well lead to productive designs for aeroelastic energy harvesters.

Acknowledgments

The authors would like to acknowledge a number of individuals for their efforts in supporting this work. Deman Tang's tireless assistance in fabricating and setting up the experiment was invaluable to the completion of this study. Moreover, the authors are heavily indebted to Dr. Tang's aeroelastic modeling codes and knowledge thereof in the formation of the computational model used in this paper. The counsel of Nigel Peake and Sevag Arzoumanian was also extremely valuable in terms of fully understanding the fluid–structure interaction of this system and working to determine the most effective methods by which to quantify the energy transfer characteristic of the flapping flag system. Alper Erturk and Dan Inman also contributed key insights regarding the electrical portions of the experimental system. The authors are grateful to these individuals for their generous gifts of time, expertise, and support.

References

Akaydin, H.D., Elvin, N., Andreopoulos, Y., 2009. Wake of a cylinder: paradigm for energy harvesting with piezoelectric materials. Experimental Fluids 49, 291–304.

Bernitsas, M., Raghavan, K., Ben-Simon, Y., Garcia, E., 2008. VIVACE (Vortex Induced Vibration Aquatic Clean Energy): a new concept in generation of clean and renewable energy from fluid flow. Journal of Offshore Mechanics and Arctic Engineering 130, 041101-1–041101-15.

Bryant, M., Garcia, E., 2010. Energy harvesting: a key to wireless sensor nodes. Proceedings of the Second International Conference on Smart Materials and Nanotechnology in Engineering 7493, 74931W–74931W-8.

Da Silva, M.C., Glynn, C., 1978. Nonlinear flexural-flexural-torsional dynamics of inextensional beam: I. Equations of motion. Mechanics Based Design of Structures and Machines 6, 437–448.

De Marqui, C., Erturk, A., Inman, D.J., 2010. Piezoaeroelastic modeling and analysis a generator wing with continuous and segmented electrodes. Journal of Intelligent Material Systems and Structures 21, 983–993.

Doaré, O., Sauzade, M., Eloy, C., 2011. Flutter of an elastic plate in channel flow: confinement and finite-size effects. Journal of Fluids and Structures 27, 76–88.

Dowell, E.H., 2004. A Modern Course in Aeroelasticity, fourth ed. Kluwer Academic Publishers, Boston.

Eichorn, C., Goldschmidtboeing, F., Woias, P., 2008. A frequency tunable piezoelectric energy converter based on a cantilever beam. In: Proceedings of PowerMEMS 2008 + microEMS2008, pp. 309–312.

Erturk, A., Vieira, W.G.R., DeMarqui, C., Inman, D.J., 2010. On the energy harvesting potential of piezoaeroelastic systems. Applied Physics Letters 96, 184103-1–184103-3.

Erturk, A., Tarazaga, P., Farmer, J., Inman, D.J., 2009. Effect of strain nodes and electrode configuration on piezoelectric energy harvesting from cantilevered beams. Journal of Vibration and Acoustics 131, 011010-1–011010-11.

Howell, R.M., Lucey, A.D., Carpenter, P.W., Pitman, M.W., 2009. Interaction between a cantilevered-free flexible plate and ideal flow. Journal of Fluids and Structures 25, 544–566.

Katz, J., Plotkin, A., 2001. Low Speed Aerodynamics, second ed. Cambridge University Press, New York.

Kimber, M., Lonergan, R., Garimella, S.V., 2009. Experimental study of aerodynamic damping in arrays of vibrating cantilevers. Journal of Fluids and Structures 25, 1334–1347.

Lindsey, K., 2002. A feasibility study of oscillating-wing power generators. Masters Thesis, Naval Postgraduate School.

Mitcheson, P.D., Yeatman, E.M., Rao, G.J., Holmes, A.S., Green, T.C., 2008. Energy harvesting from human and machine motion for wireless electronic devices. Proceedings of IEEE 96, 1457–1486.

Rosenhead, L., 1930. The effect of wind tunnel interference on the characteristics of an aerofoil. Proceedings of the Royal Society of London Series a-Containing Papers of a Mathematical and Physical Character, vol. 129; 1930, pp. 135–145.

Semler, C., Li, G., Paidoussis, M.P., 1994. The non-linear equations of motion of pipes conveying fluid. Journal of Sound and Vibration 169, 577–599.

Sodano, H., Inman, D.J., Park, G., 2004. A review of power harvesting from vibration using piezoelectric materials. The Shock and Vibration Digest 36, 197–205.

St Clair, D., Bibo, A., Sennakesavababu, V.R., Daqaq, M.F., Li, G., 2010. A scalable concept for micropower generation using flow-induced self-excited oscillations. Applied Physics Letters 96, 144103-1–144103-3.

Stanton, S., Erturk, A., Mann, B., Inman, D.J., 2010a. Nonlinear piezoelectricity in electroelastic energy harvesters: modeling and experimental identification. Journal of Applied Physics 108, 1–10.

Stanton, S., Erturk, A., Mann, B., Inman, D.J., 2010b. Resonant manifestation of intrinsic nonlinearity within electroelastic micropower generators. Applied Physics Letters 97, 254101–254103.

Stanton, S., Mann, B., in review. Nonlinear electromechanical dynamics of piezoelectric inertial generators: modeling, analysis, and experiment. Nonlinear Dynamics.

Tang, D.M., Yamamoto, H., Dowell, E.H., 2003. Flutter and limit cycle oscillations of two-dimensional panels in three-dimensional axial flow. Journal of Fluids and Structures 17, 225–242.

Tang, L., Paidoussis, M.P., Jiang, J., 2009. Cantilevered flexible plates in axial flow: energy transfer and the concept of flutter-mill. Journal of Sound and Vibration 326, 263–276.

Taylor, G.W., Burns, J.R., Kammann, S.M., Power, W.B., Welsh, T.R., 2001. The energy harvesting Eel: a small subsurface ocean/river power generator. IEEE Journal of Oceanic Engineering 26, 539–547.

Wang, D., Ko, H.H., 2010. Piezoelectric energy harvesting from flow-induced vibration. Journal of Micromechanics and Microengineering 20, 025019-1–025019-9.